ACS OMEGA

Article

Synthesis of Cu-Doped Mn₃O₄@Mn-Doped CuO Nanostructured Electrode Materials by a Solution Process for High-Performance Electrochemical Pseudocapacitors

Hasi Rani Barai, Nasrin Siraj Lopa, Faiz Ahmed, Nazmul Abedin Khan, Sajid Ali Ansari, Sang Woo Joo,* and Md. Mahbubur Rahman*

Cite This: ACS Omega 2020, 5, 22356−22366

Read Online

ACCESS | Metrics & More | Article Recommendations | SI Supporting Information

ABSTRACT: Cu-doped Mn_3O_4 and Mn-doped CuO (CMO@MCO) mixed oxides with isolated phases together with pristine Mn_3O_4 (MO) and CuO (CO) have been synthesized by a simple solution process for applications in electrochemical supercapacitors. The crystallographic, spectroscopic, and morphological analyses revealed the formation of all of the materials with good crystallinity and purity with the creation of rhombohedral-shaped MO and CMO and a mixture of spherical and rod-shaped CO and MCO nanostructures. The ratio of CMO and MCO in the optimized CMO@MCO was 2:1 with the Cu and Mn dopants percentages of 12 and 15%, respectively. The MO-, CO-, and CMO@MCO-modified carbon cloth (CC) electrodes delivered the specific capacitance (C_s) values of 541.1, 706.7, and 997.2 F/g at

5 mV/s and 413.4, 480.5, and 561.1 F/g at 1.3 A/g, respectively. This enhanced C_s value of CMO@MCO with an energy density and a power density of 78.0 Wh/kg and 650.0 W/kg, respectively, could be attributed to the improvement of electrical conductivity induced by the dopants and the high percentage of oxygen vacancies. This corroborated to a decrease in the optical band gap and charge-transfer resistance (R_{ct}) of CMO@MCO at the electrode/electrolyte interface compared to those of MO and CO. The net enhancement of the Faradaic contribution induced by the redox reaction of the dopant and improved surface area was also responsible for the better electrochemical performance of CMO@MCO. The CMO@MCO/CC electrode showed high electrochemical stability with a C_s loss of only ca. 4.7%. This research could open up new possibilities for the development of doped mixed oxides for high-performance supercapacitors.
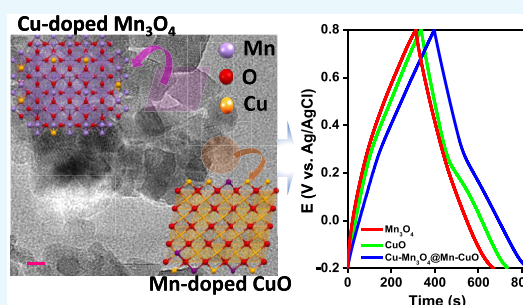
■ INTRODUCTION

The rapid advancement of nanoscale technologies has prompted the demand and widespread applications of high-performance energy storage devices, including portable electronics, electric vehicles, personal computers, off-grid homes and inverters, and energy management.[1] To date, significant efforts have been made for constructing high-performance energy storage devices (e.g., batteries, super-capacitors, and fuel cells) by developing new nanomaterials, ideas, and chemistries.[2,3] Among the energy storage technologies, an electrochemical supercapacitor (ESC) is widely recognized due to its high power density (P_d) and intermediate energy density (E_d) between the battery and conventional capacitors.[2,3] Additionally, ESC has a long cycle life, good reversibility, a wide range of operational temperatures, and high safety.[4] Based on the principles of the charge storage mechanism, ESCs can be categorized as an electric double-layer capacitor (EDLC) and a pseudocapacitor.[5,6] In EDLC, energy is stored by reversible adsorption of ions in a non-Faradaic process.[5,6] In contrast, pseudocapacitors store the charges by the Faradaic process occurring at the electrode surface.[5−7] Carbon-based materials (e.g., graphene, carbon

nanotubes, graphitic carbon nitride, etc.)[4,8] are commonly used electrode materials for the development of EDLCs with high cycling stability and long lifetime. Nevertheless, the specific capacitance (C_s) of carbon-based EDLCs significantly relies on the surface area and the pore size distribution of carbon, which is usually in the range of 78−100 and 109−201 F/g, respectively, for commercial-grade carbons and activated carbon, while these values are 222.3 and 231 F/g, respectively, for carbon nanosheets derived from *Syzygium cumini* leaves and $NaHCO_3$-activated nitrogen-doped carbon.[9,10] This limits the E_d of EDLCs much lower than that of batteries. Pseudocapacitors gained much attention to improve the C_s and E_d comparable to batteries, where the charge is stored into the surface and subsurface layers of electrochemically redox-active
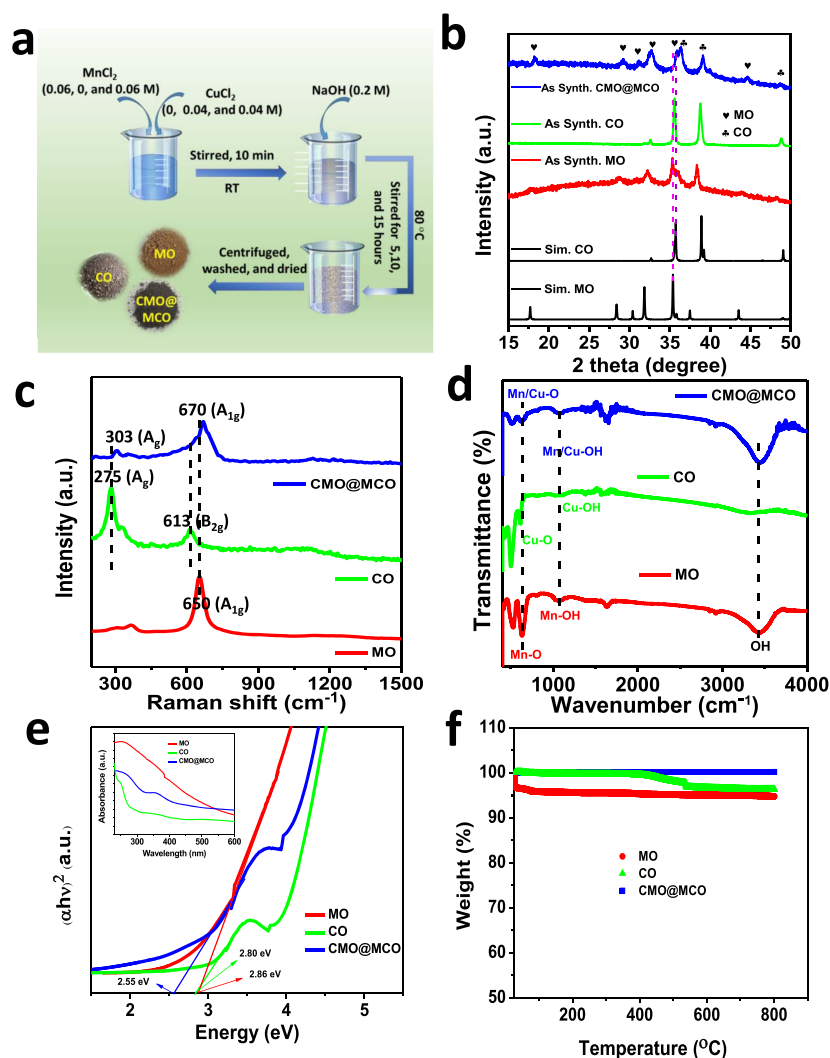
Figure 1. (a) Schematic of the synthesis of MO, CO, and CMO@MCO. (b) XRD patterns of as-synthesized MO, CO, and CMO@MCO together with the simulated XRD patterns of MO and CO. (c) Raman spectra; (d) Fourier transform infrared (FTIR) spectra; (e) Tauc's plots (the inset shows the corresponding UV−visible absorption spectra); and (f) TGA plots of MO, CO, and CMO@MCO.

materials.[11,12] The commonly used nanomaterials for the development of pseudocapacitors are transition-metal oxides (TMOs) (e.g., MnO_2, Mn_2O_3, Cu_xO, RuO_2, PbO_2, etc.),[13,14] binary transition-metal oxides (BTMOs),[15] metal nitrides/carbides/hydroxides/sulfides, and conducting polymers.[2,16−22]

In particular, TMOs are promising and widely investigated electrode materials for the development of pseudocapacitors.[13,14] This is due to their low cost, high chemical stability, and high theoretical C_s, while a few of them are toxic and expensive (e.g., RuO_2, PbO_2, etc.).[23,24] However, most of them exhibit low electrical conductivities and poor electrochemical cycling stabilities induced by the redox reactions that occur on the electrode surface.[25] For instance, the theoretical C_s values of MnO_2, Mn_3O_4, and CuO are 1233, 1400, and 1783 F/g, respectively,[3,26,27] while the electrical conductivities of Mn_3O_4 and MnO_2 are in the range from ca. 10^{-7} to 10^{-8} and 10^{-5} to 10^{-6} S/cm, respectively, and that of CuO is ca. 7.8×10^{-4} S/cm.[26,28,29] These low conductivity values of them mostly limit the practically obtainable C_s values much lower than their theoretical C_s values. For example, the reported C_s value of pristine Mn_3O_4 nanostructures is 210 F/g (at 0.5 A/g),[26] which is only ca. 15% of its theoretical C_s. Again, the reported

obtainable C_s values of three-dimensional CuO frameworks and flower-shaped CuO nanostructures were ca. 431 (at 3.5 mA/cm^2) and 296 F/g (at 0.7 A/g), respectively.[30,31] Additionally, TMOs cannot possess sufficient electroactive species with multiple oxidation states for improved Faradaic reactions to obtain high C_s.

Numerous strategies have been attempted to enhance the practical C_s values of TMOs by increasing the electrical conductivity and redox behavior, comprising the synthesis of BTMOs/mixed metal oxides/ternary metal oxides, controlling the size and morphologies, and the preparation of composites with highly conductive materials.[15,27,32−34] Recently, BTMOs that showed enhanced pseudocapacitive performance than the corresponding single-component oxides, including Ni−Co, Sr−Cu, Mn−Fe, and Mn−Cu oxides, have attracted much attention.[25,26,35,36] This can be attributed that the binary metal ions with multiple oxidation states in BTMOs can exhibit improved Faradaic redox reactions and high electrical conductivity, which is beneficial to obtain high C_s and E_d.[25,27] Even if the reported BTMOs can deliver high C_s compared to the single-component oxides prepared under similar experimental conditions, the C_s values of these BTMOs
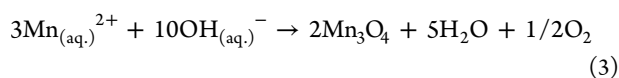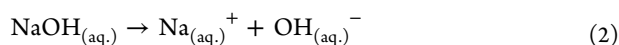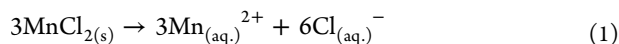
are significantly lower compared to the theoretical C_s values of single-component oxides. For example, Yuan et al. prepared Ru–Cr-based BTMOs that delivered the C_s only 148 F/g,[37] which is very low compared to the theoretical C_s of RuO_2 (1400–200 F/g) and Cr_3O_4 (3560 F/g).[38,39] In another report, Zhu et al. synthesized Mn–Cu-based BTMOs, which showed the C_s of only 422 F/g.[36] The C_s values of these Mn–Cu-based BTMOs are much lower compared to those of the reported pristine Mn-oxides and Cu oxides.[3,26,27] Since BTMOs exhibited much improved Faradaic redox behavior than TMOs, the low C_s values of them might be due to their low conductivities. Thus, the development of novel BTMOs/mixed oxides with high electrical conductivity, multiple oxidation states, and improved Faradaic redox behavior is of great importance for the development of high-performance ESCs.

Doping of BTMOs/mixed oxides is an effective strategy to enhance the electrical conductivities and C_s.[27,40] This is because a suitable dopant with an optimized doping level can form a new energy level within the band gap (E_g) of BTMOs/mixed oxides.[40] Doping can induce the formation of crystal defects by the creation of oxygen vacancies, which can enhance the net electrical conductivities of BTMOs/mixed oxides as well as electrochemical performance.[27,41] Furthermore, dopant ions itself can undergo electrochemical redox reactions, contributing to enhancing the net Faradaic contribution in ESCs.[42] Our research group developed Ca- and K-doped Sr–Cu based BTMOs, which showed improved redox activity and electrical conductivity upon doping.[27,40] Concurrently, the Ca- and K-doped Sr–Cu oxides could deliver the C_s values of ca. 308.0 and 438 F/g, respectively, while the C_s value of pristine Sr–Cu oxides was only 14.5 F/g.[27,40] Considering all of the above issues, the preparation of controlled morphologies and suitable dopant-incorporated single-phase or separate-phase mixed oxides with high theoretical C_s-based single-component oxides is essential for the development of high-performance ESCs.
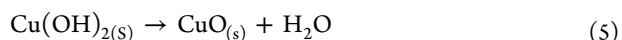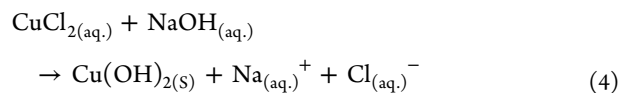
Herein, a Cu-doped Mn_3O_4 and Mn-doped CuO (CMO@MCO) mixed oxide with separate crystal phases was prepared by a simple, controllable, and scalable solution process. For comparison, pristine Mn_3O_4 (MO) and CuO (CO) were also synthesized under similar experimental conditions. The as-synthesized MO, CO, and CMO@MCO exhibit good crystallinity and purity with high oxygen vacancies. The incorporation of high percentages of Cu^{2+} and $Mn^{2+/3+}$ dopants in CMO@MCO can significantly enhance the C_s and E_d compared to those of MO and CO. The materials also showed good capacity retention with low charge-transfer resistance (R_{ct}) at the electrode/electrolyte interface.

■ RESULTS AND DISCUSSION

Figure 1a shows the schematic of the synthesis of MO, CO, and CMO@MCO (details described in the Experimental Section). The reaction mechanism for the formation of MO by reacting $MnCl_2$ with NaOH can be described as follows[43]

$$3MnCl_{2(s)} \rightarrow 3Mn_{(aq.)}^{2+} + 6Cl_{(aq.)}^{-} \qquad (1)$$

$$NaOH_{(aq.)} \rightarrow Na_{(aq.)}^{+} + OH_{(aq.)}^{-} \qquad (2)$$

$$3Mn_{(aq.)}^{2+} + 10OH_{(aq.)}^{-} \rightarrow 2Mn_3O_4 + 5H_2O + 1/2O_2 \qquad (3)$$

while the reaction mechanism for the synthesis of CO by reacting $CuCl_2$ with NaOH can be presented as follows[44]

$$CuCl_{2(aq.)} + NaOH_{(aq.)}$$
$$\rightarrow Cu(OH)_{2(S)} + Na_{(aq.)}^{+} + Cl_{(aq.)}^{-} \qquad (4)$$

$$Cu(OH)_{2(S)} \rightarrow CuO_{(s)} + H_2O \qquad (5)$$

During the synthesis of CMO@MCO, Cu^{2+} and $Mn^{2+/3+}$ can be doped into MO and CO, respectively, in three different ways: (I) substitution of $Mn^{2+/3+}$ by Cu^{2+} in MO and the substitution of Cu^{2+} by $Mn^{2+/3+}$ in CO, (II) bonding with oxygen, and (III) as a secondary phase.[40] Figure 1b displays the X-ray diffraction (XRD) patterns of as-prepared MO, CO, and CMO@MCO together with the simulated XRD patterns of MO and CO. The XRD patterns of MO and CO perfectly match with their simulated XRD patterns. The diffraction peaks of MO located at 2θ angle values of ca. 17.62, 28.53, 31.95, 35.20, 35.70, 38.10, and 43.75° correspond to the crystallographic planes of tetragonal Mn_3O_4 with the hkl reflections of (101), (112), (103), (211), (202), (004), and (220), respectively,[26] while the major diffraction peaks of CO located at 2θ angle values of ca. 35.65, 38.75, and 49.05° resemble the hkl reflections of (110), (200), and (20$\bar{2}$), respectively.[31] The sharp XRD peaks of both MO and CO are without the existence of any additional peaks, indicating their high crystallinity with high purity. In contrast, the XRD pattern of CMO@MCO exhibits the presence of all of the major peaks of MO and CO without the existence of any secondary phase peaks. All of the XRD peaks of CMO@MCO are substantially shifted to a higher 2θ angle values compared to those of MO and CO, indicating the formation of separate-phase mixed oxides of MO and CO upon doping of Cu and Mn, respectively.[27,40] For example, the 2θ angle values of major diffraction peaks of MO for (211) and (202) planes were shifted to about 0.40 and 41°, respectively, while this shifting was 0.45 and 0.30°, respectively, for (200) and (20$\bar{2}$) planes of CO. This shifting of the XRD peaks in CMO@MCO can be ascribed to the decrease of the lattice parameter/unit cell volume induced by the substitution of $Mn^{2+/3+}$ by Cu^{2+} in CMO and Cu^{2+} by $Mn^{2+/3+}$ in MCO.[27,40] Since the ionic radii of Mn^{2+} (70 pm) and Mn^{3+} (72 pm) in mixed-valence MO are similar to the ionic radius of Cu^{2+} (73 pm) in CO, the doping of Cu^{2+} and $Mn^{2+/3+}$ in CMO@MCO mostly occurs by the substitution of $Mn^{2+/3+}$ by Cu^{2+} in CMO and Cu^{2+} by $Mn^{2+/3+}$ in MCO. However, both $Mn^{2+/3+}$ and Cu^{2+} can also be partially inserted into CMO@MCO by binding with oxygen.

Raman spectra of the compounds were measured for further analyses of the compositions and crystal structures, as shown in Figure 1c. The Raman spectrum of MO exhibits three characteristics major band peaked at ca. 303, 365, and 650 cm^{-1}, which is close to the reported values of hausmannite MO.[45] The high-intensity band of MO at 650 cm^{-1} can be attributed to the A_{1g} symmetric stretching of Mn–O in octahedral MnO_6 units, specifying the formation of MO with high crystallinity and purity.[46] The Raman bands of CO located at ca. 275, 327, and 613 cm^{-1} can be ascribed to the A_g, B_{1g}, and B_{2g} vibration modes, respectively.[47] These values well match with the reported results,[47,48] indicating the formation of CO with good crystallinity. CMO@MCO shows the characteristics high-intensity A_{1g} band of MO at ca. 670 cm^{-1} and A_g and B_{2g} bands of CO at ca. 303 and 635 cm^{-1}, respectively. This blue shifting of the major Raman bands of
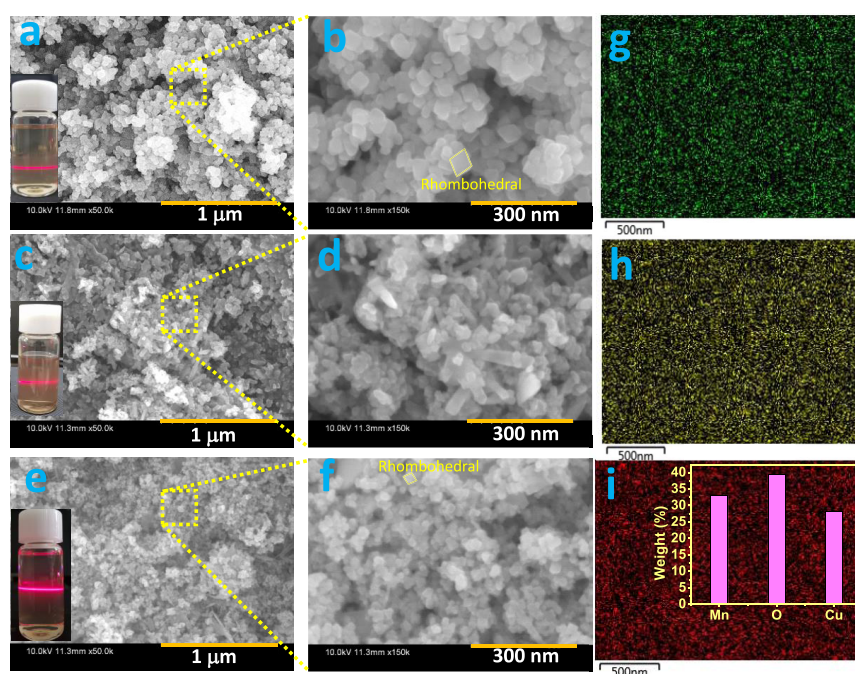
Figure 2. FE-SEM images of (a, b) MO, (c, d) CO, and (e, f) CMO@MCO. EDS elemental mapping of (g) Mn, (h) O, and (i) Cu in CMO@MCO (the inset shows the elemental weight (%) of Mn, O, and Cu). Insets of (a), (c), and (e) present the photographic images of Tyndall light scattering experiments of MO, CO, and CMO@MCO, respectively.

MO and CO in CMO@MCO can be ascribed to the local structure distortion of MO and CO induced by doping.[45,47] Besides, the intensity reduction with the broadening of the major peaks demonstrates the occurrence of lattice defects by the creation of oxygen vacancies.[45] These results further specify the formation of MO, CO, and CMO@MCO with good crystallinity, which is consistent with the XRD results.

Figure 1d presents the FTIR spectra of MO, CO, and CMO@MCO. The IR absorption bands of MO at ca. 630, 527, and 410 cm^{-1} correspond to the coupling modes between the Mn−O stretching of tetrahedral and octahedral sites.[49] These stretching vibrations of Cu−O in the CO were located at ca. 609, 501, and 421 cm^{-1}. The FTIR spectra of CMO@MCO also show similar stretching vibrations of Mn−O and Cu−O at ca. 625, 515 cm^{-1}. All of the materials exhibit the common weak band of metal (Mn, Cu)−OH vibration at ca. 1070 cm^{-1} together with weak and strong bands of O−H vibration arising from the adsorbed water molecules at ca. 1630 and 3450 cm^{-1}, respectively.[49,50] No other impurity band was observed in the materials, indicating the effective synthesis of MO, CO, and CMO@MCO.

The optical E_g was calculated using UV−visible absorption spectra (inset of Figure 1e), which were measured after dispersing the materials in ethanol by sonication. Figure 1e shows the Tauc plots of MO, CO, and CMO@MCO, which revealed the E_g values of ca. 2.86, 2.80, and 2.55 eV, respectively. The decrease in the E_g of CMO@MCO compared to those of MO and CO can be ascribed to the formation of energy levels inside the E_g adjacent to the conduction band of CMO@MCO, which is consistent with the reported literature.[51] This result suggests that CMO@MCO has high electrical conductivity than MO and CO, which is beneficial to obtain high C_s. All of the materials showed high thermal stability up to 800 °C with the weight loss of only ca. 5.35, 3.5, and 0.1 wt % for MO, CO, and CMO@MCO,

respectively, as shown in Figure 1f. This small percent of weight loss for MO and CO possibly occurs due to the loss of chemisorbed or physisorbed water molecules, which is consistent with the reported results.[52,53] The negligible weight loss for CMO@MCO can be attributed to the higher melting points of Cu (1085 °C) and Mn (1246 °C) dopants, while both dopants also possibly act as stabilizing agents for improving the thermal stability of CMO@MCO.[54,55] The Brunauer−Emmett−Teller (BET) surface area (SA$_{BET}$) was measured using the BET equation by measuring the N$_2$ adsorption−desorption isotherm (Figure S1). All of the materials exhibit the IUPAC-classified type-IV isotherms with the SA$_{BET}$ values of ca. 41.10, 55.95, and 56.0 m^2/g, respectively, for MO, CO, and CMO@MCO.

Figure 2a,b shows the field-emission scanning electron microscopy (FE-SEM) images of MO, which revealed the formation of homogeneous and uniform-sized, well-defined, rhombohedral-shaped nanostructures with an average edge length of ca. 40 nm. Under the similar synthesis process, CO shows the formation of mixed morphologies of nanoparticles (average diameter of ca. 25 nm) and nanorod-type structures (Figure 2c,d). The FE-SEM images of CMO@MCO display mostly the mixed morphologies of well-defined rhombohedra and nanoparticles, as presented in Figure 2e,f. The nanoparticles size (ca. 20 nm) and the average edge length of the rhombohedra (ca. 30 nm) were reduced in CMO@MCO compared to those in MO and CO, which is advantageous to obtain high surface area and electrochemical performance. The formation of nanoscale size range MO, CO, and CMO@MCO was further confirmed by the Tyndall scattering experiments of their respective dispersed solutions, as shown in the insets of Figure 2a, c, and e, respectively. Figure 2g−i displays the energy-dispersive X-ray spectrometry (EDS) elemental mapping of Mn, O, and Cu, respectively, in CMO@MCO. The corresponding EDS spectrum is shown in Figure S2. This
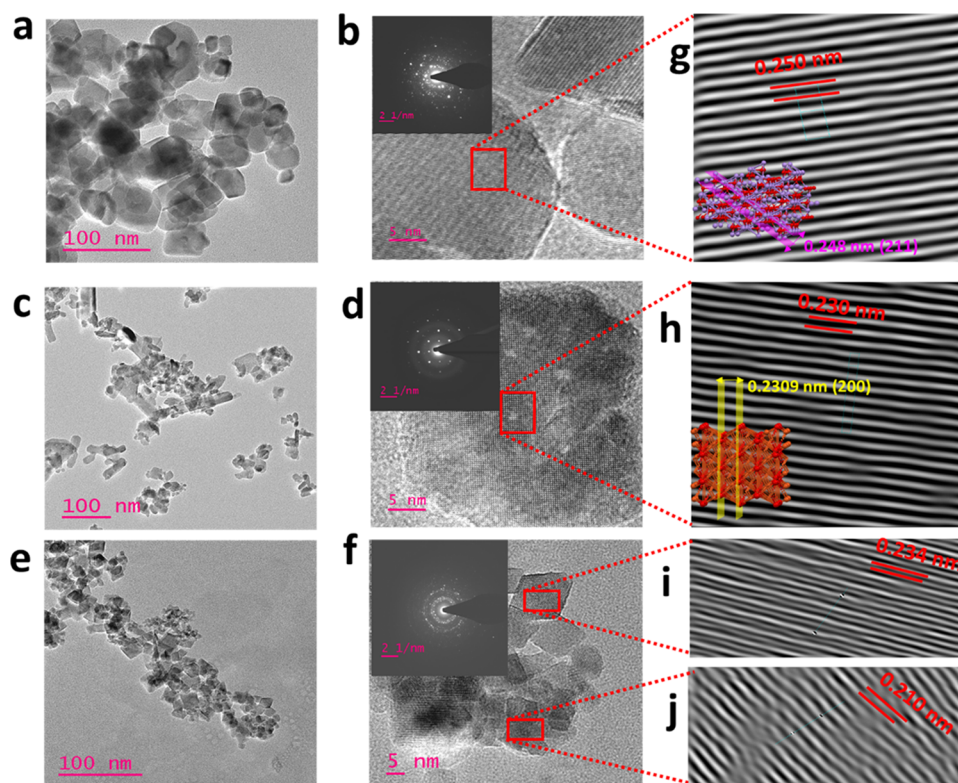
Figure 3. HR-TEM images of (a, b) MO, (c, d) CO, and (e, f) CMO@MCO. Insets of (b), (d), and (f) show the SAED patterns of MO, CO, and CMO@MCO, respectively. Magnified calibrated lattice fringes of (g) MO (the inset shows the interplanar spacing of the (211) plane), (h) CO (the inset shows the interplanar spacing of the (200) plane), and (i, j) CMO@MCO.
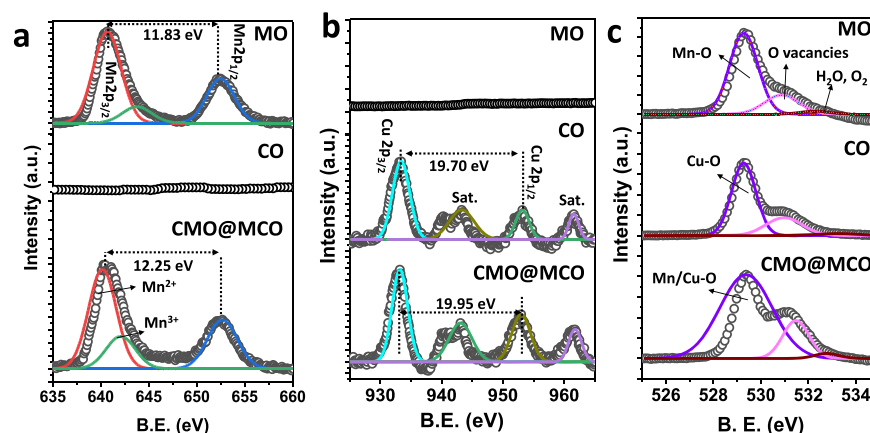

Figure 4. Core-level XPS spectra of (a) Mn 2p, (b) Cu 2p, and (c) O 1s in MO, CO, and CMO@MCO. The open circles and solid lines designate the experimental and fitted data, respectively.

result indicates the homogeneous distribution of Mn, O, and Cu with the elemental weights (%) of ca. 32.45, 39.29, and 28.26%, respectively (inset of Figure 2i).

The morphologies of MO, CO, and CMO@MCO were further analyzed by high-resolution-transmission electron microscopy (HR-TEM), as displayed in Figure 3a−f, respectively. All of the HR-TEM images showed transparency to the electron beam, indicating the formation of non-aggregated nanostructures. The morphologies, shapes, and sizes of the nanostructures obtained from the HR-TEM images well match with the FE-SEM images. The selected area electron diffraction (SAED) patterns of MO, CO, and CMO@MCO (insets of Figure 3b,d,f, respectively) displayed bright spots with bright rings, suggesting the high crystallinity of the

materials,[27,40] and this was consistent with the XRD patterns. The magnified calibrated lattice fringes of MO (Figure 3g) for the crystal plane of (211) revealed an interplanar spacing of ca. 0.250 nm, while it was ca. 0.230 nm for CO (Figure 3h) for the crystal plane of (200). These results well match with the *d*-spacing values of MO and CO obtained from the XRD patterns (0.248 and 0.230 nm, respectively).[42,56] The interplanar spacings of the (211) plane of MO and the (200) plane of CO were reduced to ca. 0.234 and 0.210 nm, respectively, in CMO@MCO. The reduction of the interplanar spacing in CMO@MCO is in good agreement with the shifting of the XRD peaks, indicating the successful formation of Cu-doped MO and Mn-doped CO mixed oxides.
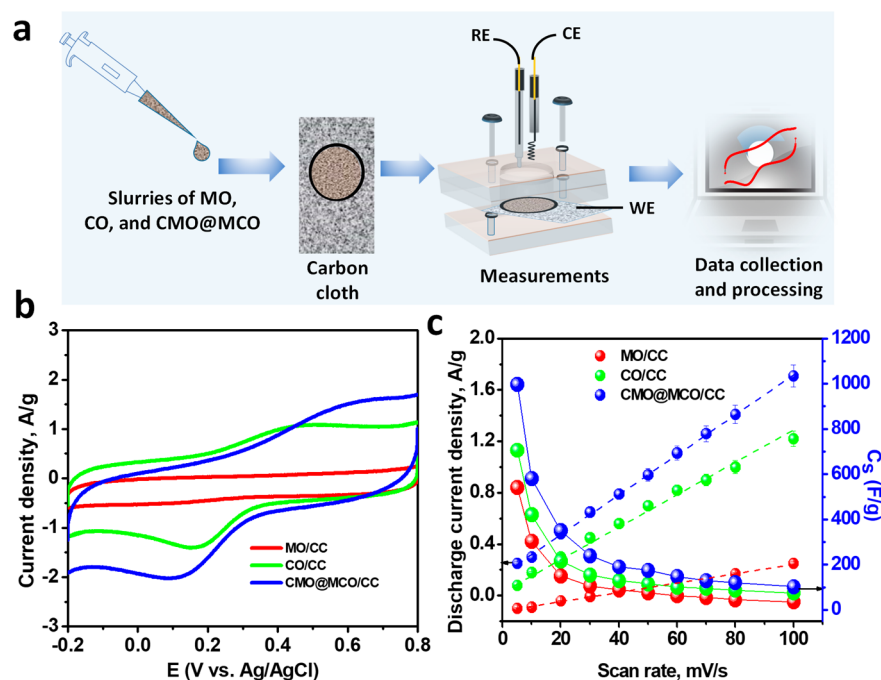
Figure 5. (a) Schematic illustrations of the fabrication of MO/, CO/, and CMO@MCO/CC electrodes and electrochemical measurements. (b) CVs of the MO/, CO/, and CMO@MCO/CC electrodes at a scan rate of 100 mV/s. (c) Discharge current density vs scan rate and C_s vs scan rate plots of the electrodes.

The elemental compositions and oxidation states of the materials were characterized by X-ray photoelectron spectroscopy (XPS) measurements. Figure S3 presents the XPS survey spectra of MO, CO, and CMO@MCO. The XPS spectrum of MO shows the existence of characteristics elemental peaks of Mn 3p, Mn 3s, Mn 2p, and O 1s,[57] while CO also exhibits the presence of the elemental peaks of Cu 3p, Cu 3s, Cu 2p, and O 1s.[31] As anticipated, the elemental peaks of Mn 3p, Mn 3s, Mn 2p, Cu 3p, Cu 3s, Cu 2p, and O 1s are present in CMO@MCO. Additionally, all of the compounds displayed an additional peak of C 1s, which might be arising from the ubiquitous carbon contamination. Figure 4a−c shows the high-resolution XPS spectra of Mn 2p, O 1s, and Cu 2p in MO, CO, and CMO@MCO, respectively. The unfitted doublet peaks of Mn $2p_{3/2}$ and Mn $2p_{1/2}$ in the core-level Mn 2p spectrum of MO were located at ca. 640.62 and 652.45 eV, respectively, with a separation of 11.83 eV. This larger doublet separation can be attributed to the weak interaction of different ion sites.[58] The deconvoluted Mn $2p_{3/2}$ spectrum shows two-component peaks centered at ca. 640.65 and 643.90 eV, indicating that the oxidation states of Mn are +2 and +3 in MO.[58] As expected, no obvious Mn 2p peak was observed in CO, while the unfitted doublet peaks of Mn $2p_{3/2}$ and Mn $2p_{1/2}$ in the core-level Mn 2p spectrum of CMO@MCO were located at ca. 640.35 and 652.60 eV, respectively, with a separation of 12.25 eV. This shifting of the doublet with an increase of peak separation can be ascribed to the electron transfer between MO and CO in CMO@MCO induced by the dopants.[58] The deconvoluted Mn $2p_{3/2}$ spectrum in CMO@MCO displays two-component peaks located at ca. 640.65 and 643.90 eV, indicating that the oxidation states of Mn ions are +2 and +3.[58] The integral area of the Mn^{2+} component spectrum was almost unchanged, while the intensity and the integral area of Mn^{3+} were ca. 15% higher in CMO@MCO than those in MO. This designates that heterovalent Mn^{3+} is

the main dopant in CO of CMO@MCO, which is beneficial to create lattice defects by the creation of oxygen vacancies. The high-resolution Cu 2p spectrum exhibits the doublet peaks of Cu $2p_{3/2}$ and Cu $2p_{1/2}$, which were at ca. 933.40 and 953.10 eV, respectively, in CO, and ca. 933.10 and 953.05 eV, respectively, in CMO@MCO. The double separation of Cu 2p in CO was ca. 19.70 eV, while it was ca. 19.95 eV in CMO@MCO. This 0.25 eV increase of the separation can be ascribed to the electron transfer between the metal oxide components and the dopants.[58] Additionally, Cu 2p spectra of CO and CMO@MCO exhibit high-intensity satellite peaks of Cu $2p_{3/2}$ at ca. 943.50 and 943.10 eV, respectively, and Cu $2p_{1/2}$ at ca. 961.74, and 961.75 eV, respectively. This suggests that the oxidation state of Cu in CO and CMO@MCO is +2.[31] The Cu $2p_{3/2}$ component spectrum was ca. 12% higher in CMO@MCO compared to that in CO, suggesting the incorporation of the Cu^{2+} dopant in CMO@MCO. The ratio of the integral areas of Mn $2p_{3/2}$ and Cu $2p_{3/2}$ is almost 2:1. No obvious peaks of Cu 2p were observed in MO. The deconvoluted core-level spectra of O 1s in MO, CO, CMO@MCO present three-component peaks. The high-intensity peak at a lower binding energy of ca. 529.27 eV can be ascribed to the binding energies of the metal−oxygen bond.[41,59] The other low-intensity peaks at ca. 531.0 and 532.80 eV in all of the samples can be attributed to the oxygen defect/vacancies and adsorbed H_2O/O_2.[41] The intensity ratios of oxygen defects/vacancies were ca. 24, 25, and 45% compared to the intensities of metal−oxygen bonds in MO, CO, and CMO@MCO, respectively. This high percentage of oxygen vacancies in all of the materials can function as active sites for improved Faradaic redox reactions with high capacitive performance.[59] This result further suggests that doping can enhance the oxygen vacancies in CMO@MCO, which is in well agreement with Raman observations.

Figure S4 presents the XRD patterns of CMO@MCO prepared with the reaction times of 5 and 15 h without altering

Table 1. Supercapacitive Performance Comparison of Some Reported Metal Oxide Nanostructures with the Current MO, CO, and CMO@MCO Nanostructured Materials

electrode materials	method	electrode system	applied current/scan rate	C_s (F/g)	ref
NiCo$_2$O$_4$−NiO nanoflowers	CD	asymmetric two-electrode	1 A/g	82.1	25
Mn$_3$O$_4$ micropillars/walls	CD	three-electrode	0.5 A/g	210	26
Sr$_{0.9}$Ca$_{0.1}$Cu$_2$O$_2$ nanostructures	cv three-electrode	three-electrode	0.47 A/g	308.0	27
3D nanoporous CuO	CD	symmetric two-electrode	3.5 mA/cm^2	431	30
Ni/CuO nanoplates	CD	three-electrode	2 A/g	535	31
Cu/CuO nanobuds	CD	three-electrode	0.7 A/g	230	31
Cu/CuO nanoflowers	CD	three-electrode	0.7 A/g	296	31
Mn90Fe10 oxide	CV	three-electrode	5 mV/s	255	35
Mn−Cu binary oxides nanostructures	CV	symmetric two-electrode	0.5 A/g	417	36
Cu-doped Mn$_3$O$_4$ hollow structures	CD	asymmetric two-electrode	1 A/g	305	42
Cr-doped Mn$_3$O$_4$ nanocrystals	CD	three-electrode	0.5 A/g	272	58
CuO nanosheets	CD	three-electrode	1 A/g	418	60
Ag-doped CuO nanosheets	CD	three-electrode	10 A/g	299	60
Mn$_3$O$_4$ nanoparticles/MWCNT composites	CV	three-electrode	5 mV/s	420	61
MO, CO, and CMO@MCO nanostructures	CV	three-electrode	5 mV/s	541.1, 706.7, and 997.2, respectively	this work
	CD		1.3 A/g	413.4, 480.5, and 561.1, respectively	
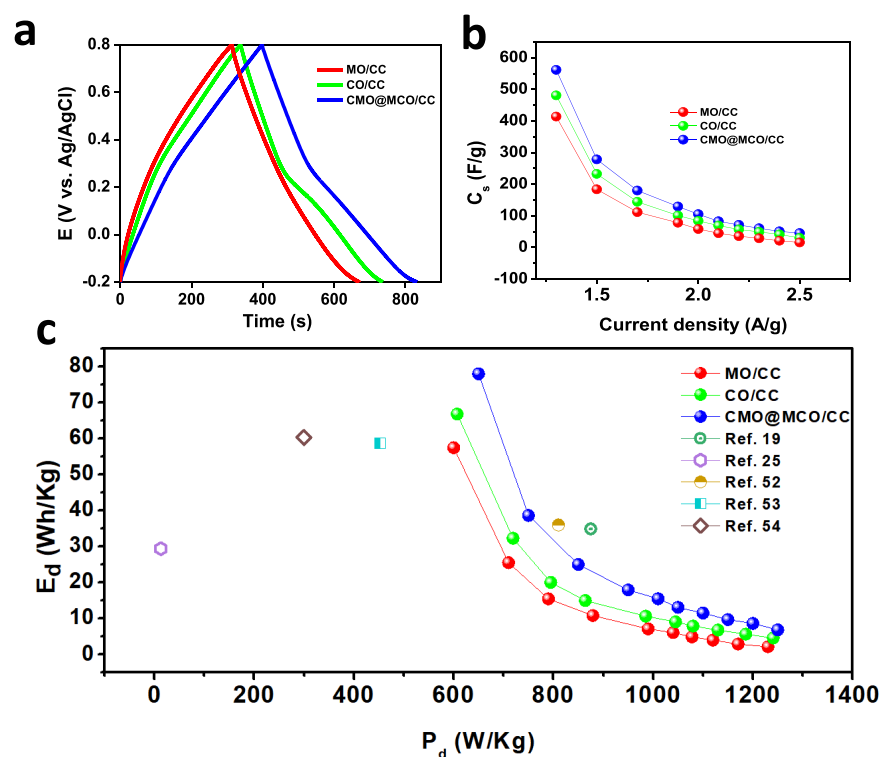
Figure 6. (a) CD plots of MO/, CO/, and CMO@MCO/CC electrodes at a current density of 1.3 A/g. (b) C_s vs current density and (c) E_d vs P_d plots of the electrodes with varying applied current densities compared with those of the other reported materials.

the compositions of precursors, which was prepared for the optimization of the best-performed electrode. Both the XRD patterns well match with the XRD pattern of CMO@MCO prepared with the reaction time of 10 h. Figure 5a shows the schematic of the fabrication of MO/, CO/, and CMO@MCO/CC electrodes (details presented in the Experimental Section). The electrochemical behavior of the modified electrodes was investigated by cyclic voltammetry (CV) in the KCl$_{(aq.)}$ (1 M)

solution. Figure S5 shows the CVs of CMO@MCO-modified electrodes with the synthesis times of 5, 10, and 15 h. The CMO@MCO prepared with the synthesis time of 10 h has the highest discharge current density, which is considered as the optimal electrode material for further application and characterization. Figure 5b shows the CVs of MO/, CO/, and the optimized CMO@MCO/CC electrodes at a scan rate of 100 mV/s. The CVs of these electrodes at other scan rates
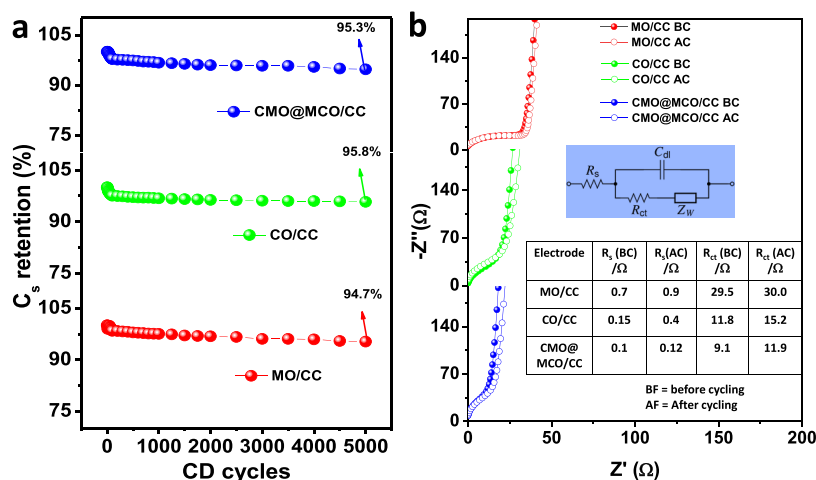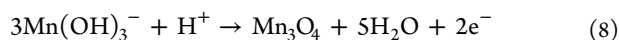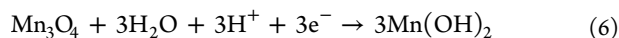
Figure 7. (a) C_s retention vs CD cycles (5000 cycles) plots of the electrodes at an applied current density of 2.5 A/g. (b) Nyquist plots of MO/, CO/, CMO@MCO/CC electrodes before and after CD cycling (5000 cycles) measured under open-circuit conditions. The inset shows the Randles equivalent circuit model to fit the EIS spectra, where C_{dl} is the double-layer capacitance. The table in the inset summarizes the EIS parameters of the electrodes before and after CD cycling.

(5−80 mV/s) are shown in Figure S6. The CV curves of the MO/CC electrode were of a nearly rectangular shape, consistent with the reported results.[42,58] The pseudocapacitive energy storage mechanism with low redox property of MO can be explained according to the following proton−electron transfer reactions (reactions 6−8). Furthermore, the intercalation/deintercalation of K^{+} into the tunnels of MO (Figure S7) is also contributing to the energy storage process.

$$Mn_3O_4 + 3H_2O + 3H^+ + 3e^- \rightarrow 3Mn(OH)_2 \quad (6)$$

$$Mn(OH)_2 + H_2O \rightarrow Mn(OH)_3^- + H^+ \quad (7)$$

$$3Mn(OH)_3^- + H^+ \rightarrow Mn_3O_4 + 5H_2O + 2e^- \quad (8)$$

The redox behavior and the reversibility were enhanced for both CO/CC and CMO@MCO/CC electrodes with the anodic and cathodic peak potentials of ca. 0.45 and 0.16 V, respectively, for the CO/CC electrode, while these values were ca. 0.63 and 0.11 V, respectively, for the CMO@MCO/CC electrode. The appearance of well-defined redox peak in both CO and CMO@MCO can be ascribed to the involvement of the redox reaction between Cu^{2+} and Cu^{+} according to the following reaction (reaction 9).[44] Moreover, the intercalation/deintercalation of K^{+} into the tunnels of CO (Figure S8) and CMO@MCO and the redox reaction of the Cu^{2+} dopants (reaction 10)[42] in CMO@MCO are also contributing in the energy storage process.

$$CuO + 1/2 H_2O + e^- \leftrightarrow 1/2 Cu_2O + OH^- \quad (9)$$

$$Cu^{2+} (doped) + e^- \leftrightarrow Cu^+ \quad (10)$$
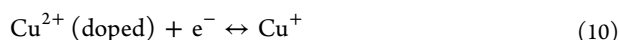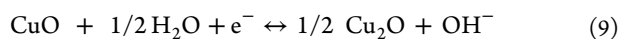
The discharge current density of all of the electrodes showed a linear behavior with the scan rates (Figure 5c), demonstrating a faster charge−discharge (CD) process with good reversibility. From the CV plots, the C_s at different scan rates were measured according to equation SI.[2] The C_s values of the MO/CC and CO/CC electrodes were ca. 541.1 and 706.7 F/g, respectively, at a scan rate of 5 mV/s, which decreased with increasing scan rates (Figure 5c). This is consistent with the usual capacitive behaviors of electrode materials.[2,27,40,42] The high C_s values of MO/CC and CO/CC electrodes can be

ascribed to the improved conductivity and redox activity induced by the oxygen vacancies with enhanced K^{+} interaction/deintercalation into the tunnels of MO and CO. The C_s was enhanced to ca. 997.2 F/g in CMO@MCO at a scan rate of 5 mV/s. This substantial enhancement of C_s in CMO@MCO compared to those in MO and CO and other reported values of MO and CO nanomaterial-based electrodes (Table 1) can be attributed to the existence of higher oxygen vacancies (ca. 47 and 45% higher compared to MO and CO, respectively), lower surface area, and improved electrical conductivity with reduced E_g. Also, dopants are responsible for the improvement of C_s by enhancing the net Faradaic redox reaction.

The chronoamperometric CD method was used to analyze the capacitive performance of the electrodes. Figure 6a shows the CD plots of MO/, CO/, and CMO@MCO/CC electrodes at a discharge current density of 1.3 A/g in KCl$_{(aq.)}$ (1 M). The CD plots of all of the electrodes at other discharge current densities (1.5−2.5 A/g) are presented in Figure S9. The CD plots of the MO/CC electrode showed a nearly linear CD profile without any IR drop, as consistent with the CV results. The CD plots of CO/CC and CMO@MCO/CC electrodes exhibited a nonlinear pseudocapacitive behavior without any IR drop with a potential plateau near the similar oxidation and reduction peaks of their respective CVs. The C_s of the electrodes from the CD plots were calculated according to equation SII.[2,40] Figure 6b displays the plots of C_s vs discharge current densities. The C_s of the MO/CC and CO/CC electrodes were ca. 413.4 and 480.5 F/g, respectively, at 1.3 A/g. These values were ca. 15.6 and 30.0 F/g, respectively, at 2.5 A/g, which are higher or similar to the reported values for other MO, CO, doped MO, and doped CO nanomaterial-based ESCs (Table 1). The higher C_s value of CO/CC compared to that of MO/CC can be ascribed to the higher electrical conductivity and oxygen vacancy of CO compared to those of MO. In contrast, the C_s values of the CMO@MCO/CC electrode were ca. 561.1 and 45 F/g at the current densities of 1.3 and 2.5 A/g, respectively. This substantial enhancement of the C_s value of CMO@MCO than those of MO and CO can be ascribed to the much higher oxygen vacancies, higher surface area due to the smaller particle size,

and improved electrical conductivity of CMO@MCO, which is consistent with the morphological, E_g, and XPS analyses. This result further suggests that the controlled percentage of doping in CMO@MCO has a negligible influence on the K$^+$ intercalation/deintercalation into the tunnels of CMO and CMO, even if doping induces to decrease the size of tunnels by decreasing the lattice parameter/unit cell volume. The E_d and P_d of the electrodes were calculated according to equations SIII and SIV, respectively.[27,40] Figure 6c summarizes the Ragone plot (E_d vs P_d) of all of the electrodes. The E_d values of the MO/, CO/, and CMO@MCO/CC electrodes were ca. 57.4, 66.8, and 78.0 Wh/kg, respectively, with the P_d values of 600.0, 607.1, and 650.1 W/kg, respectively, at a current density of 1.3 A/g. When the P_d was close to 1000 W/kg, the E_d values of these electrodes were ca. 7.1, 10.7, and 15.5 Wh/kg, respectively. The E_d values of these electrodes are much higher compared to those of reported other metal-oxide-based electrode materials, as summarized in Figure 6c. This result further designates that CMO@MCO is a promising electrode material for the commercial development of ESCs with high E_d.

The long-term electrochemical stability of the materials was evaluated by cyclic CD measurements for 5000 cycles at 2.5 A/g. Figure 7a presents the C_s retention (%) of the MO/, CO/, and MCO@CMO/CC electrodes as a function of the number of CD cycles. All of the electrodes exhibit very low C_s loss (ca. 5.3, 4.2, and 4.7%, respectively) after the CD cycles, which can be attributed to their good crystallinity. The little decrease of C_s after CD cycling is perhaps due to the changes in the volume of the electrodes induced by the repeated redox reactions during cycling. The cycling stability of the electrodes was further analyzed by electrochemical impedance spectra (EIS). Figure 7b shows the EIS plots of the electrodes before and after CD cycling, and the corresponding EIS parameters are summarized in a table in the inset of Figure 7b. All of the EIS spectra display a well-defined semicircle in the high-frequency region due to the charge-transfer resistance (R_{ct}) at the electrode/electrolyte interface and a straight line of Warburg diffusion (Z_w) in the low-frequency region.[27,40] The very low solution resistance (R_s) of all of the electrodes demonstrate the good adhesion of the materials with the CC substrate. Before CD cycling, the R_{ct} values of the MO/, CO/, and MCO@CMO/CC electrodes were ca. 29.5, 11.8, and 9.1 Ω, respectively, while these values were ca. 30.0, 15.2, and 11.9 Ω, respectively, after CD cycling. These small variations in R_{ct} before and after CD cycling designate the high long-term stability of all of the electrode materials, which is promising for the development of highly stable ESCs.

CONCLUSIONS

In summary, Cu-doped MO and Mn-doped CO (CMO@MCO) mixed oxides with isolated phases together with pristine MO and CO were prepared by a simple solution process, exhibiting good crystallinity and purity for applications in ESCs. The optimized CMO@MCO/CC electrode with the CMO and MCO ratio of 2:1 and the Cu and Mn dopant percentages of 12 and 15%, respectively, delivered the C_s and E_d of 561.1 F/g (at 1.3 A/g) and 78.0 Wh/kg, respectively. However, these values were ca. 413.4 F/g and 57.4 Wh/kg, respectively, for MO/CC, and 480.5 F/g and 66.8 Wh/kg, respectively, for CO/CC. The electrochemical performance of CMO@MCO was much higher or comparable to that of the reported other MO, CO, doped MO, and doped CO

nanostructured electrode materials. The attained C_s of CMO@MCO was still much lower compared to the theoretical C_s of each component oxide, which could be further enhanced by controlling the morphologies and porosities of CMO@MCO. Thus, CMO@MCO is a potential electrode material for the development of high-performance ECSs as well as other electrochemical devices, including batteries and sensors. We believe that this research will guide the researchers to develop other doped mixed oxides with mixed or separate phases for ESC applications.

EXPERIMENTAL SECTION

Chemicals and Measurements. All of the chemicals were bought from Sigma-Aldrich (St Louis, MO) unless otherwise specified. Ultrapure water was used throughout the experiments. The details of the instrumentations are described in the Supporting Information. All of the characterizations of CMO@MCO described in the main text of this manuscript are achieved using optimized CMO@MCO with a synthesis time of 10 h (details of the optimization can be found in the electrochemical section).

Synthesis of MO, CO, and CMO@MCO. For the synthesis of MO, a solution of MnCl$_2$ (0.06 M) was prepared in 50 mL of water and stirred at room temperature (RT) for 10 min. Then, NaOH (0.20 M) was added to the solution in stirring conditions at RT, and the mixture was stirred at 80 °C for 10 h. After completing the reaction, the reddish-brown precipitate of MO was collected by the centrifugation method, washed with water and ethanol, and dried in an oven at 100 °C. CO was synthesized by a similar method to MO synthesis with the CuCl$_2$ and NaOH concentrations of 0.04 and 0.20 M, respectively. The as-prepared dark brown precipitate of CO was washed with water and ethanol and dried in an oven at 100 °C. For the synthesis of CMO@MCO, mixed solutions of CuCl$_2$ (0.04 M) and MnCl$_2$ (0.06 M) were prepared in 50 mL of water and stirred at room temperature (RT) for 10 min. Subsequently, NaOH (0.20 M) was added into the mixed solutions in stirring conditions at RT. The reaction mixtures were stirred at 80 °C for 5, 10, and 15 h. After completing each reaction, the brownish-black precipitates of CMO@MCO were collected by the centrifugation method, washed with water and ethanol, and dried in an oven at 100 °C.

Fabrication of Electrodes and Electrochemical Characterization. The as-synthesized MO, CO, and CMO@MCO (80 wt % each) were mixed separately with carbon black (15 wt %) and poly(vinylidene fluoride) (PVDF) (5 wt %) in 2-propanol to prepare slurries. The slurries were deposited onto the carbon cloth (CC, type B-1A, E-TEK) electrodes in an O-ring confined area and dried at room temperature for 24 h. All of the electrochemical measurements were performed with a CHI660C potentiostat/galvanostat (CH Instruments Inc.). The modified electrodes were used as a working electrode; Ag/AgCl (sat. KCl) and Pt wire were used as reference and counter electrodes, respectively. All of the electrochemical measurements were executed using KCl$_{(aq.)}$ (1 M) as an electrolyte. The electrochemical impedance spectra (EIS) spectra were measured in the frequency range between 0.1 Hz and 1 MHz with a sinusoidal wave amplitude of 10 mV, which were fitted by Z-view software (Scribner Associates Inc.).

■ ASSOCIATED CONTENT

ⓈI Supporting Information

The Supporting Information is available free of charge at https://pubs.acs.org/doi/10.1021/acsomega.0c02740.

Details of measurements, N_2 adsorption−desorption isotherms, EDS spectrum, XPS survey spectra, XRD patterns, calculation of specific capacitance, CV and CD plots, calculation of energy density and power density, and crystal structures (PDF)

■ AUTHOR INFORMATION

Corresponding Authors

Sang Woo Joo − *Department of Mechanical Engineering, Yeungnam University, Gyeongsan 38541, Korea;* ⓘ orcid.org/0000-0001-9102-4224; Email: swjoo@yu.ac.kr

Md. Mahbubur Rahman − *Department of Energy and Materials, Konkuk University, Chungju 27478, Korea;* ⓘ orcid.org/0000-0003-0012-5324; Email: mahbub1982@kku.ac.kr

Authors

Hasi Rani Barai − *Department of Mechanical Engineering, Yeungnam University, Gyeongsan 38541, Korea;* ⓘ orcid.org/0000-0001-5915-8425

Nasrin Siraj Lopa − *Department of Energy and Materials, Konkuk University, Chungju 27478, Korea*

Faiz Ahmed − *Department of Energy and Materials, Konkuk University, Chungju 27478, Korea*

Nazmul Abedin Khan − *Department of Mathematical and Physical Sciences, East West University, Dhaka 1212, Bangladesh*

Sajid Ali Ansari − *Department of Physics, College of Science, King Faisal University, Al-Ahsa 31982, Saudi Arabia*

Complete contact information is available at:
https://pubs.acs.org/10.1021/acsomega.0c02740

Notes

The authors declare no competing financial interest.

■ ACKNOWLEDGMENTS

■ REFERENCES

(1) Gür, T. M. Review of electrical energy storage technologies, materials and systems: challenges and prospects for large-scale grid storage. *Energy Environ. Sci.* **2018**, *11*, 2696−2767.

(2) Ansari, S. A.; Khan, N. A.; Hasan, Z.; Shaikh, A. A.; Ferdousi, F. K.; Barai, H. R.; Lopa, N. S.; Rahman, M. M. Electrochemical synthesis of titanium nitride nanoparticles onto titanium foil for electrochemical supercapacitors with ultrafast charge/discharge. *Sustainable Energy Fuels* **2020**, *4*, 2480−2490.

(3) Barai, H. R.; Rahman, M. M.; Rahim, A.; Joo, S. W. α-MnO_2 nanorod/boron nitride nanoplatelet composites for high-performance nanoscale dielectric pseudocapacitor applications. *J. Ind. Eng. Chem.* **2019**, *79*, 115−123.

(4) Wang, Y.; Song, Y.; Xia, Y. Electrochemical capacitors: mechanism, materials, systems, characterization and applications. *Chem. Soc. Rev.* **2016**, *45*, 5925−5950.

(5) Barai, H. R.; Rahman, M. M.; Joo, S. W. Annealing-Free Synthesis of K-doped Mixed-Phase TiO_2 Nanofibers on Ti Foil for Electrochemical Supercapacitor. *Electrochim. Acta* **2017**, *253*, 563−571.

(6) Barai, H. R.; Rahman, M. M.; Joo, S. W. Template-free synthesis of two-dimensional titania/titanate nanosheets as electrodes for high-performance supercapacitor applications. *J. Power Sources* **2017**, *372*, 227−234.

(7) Chen, Z.; An, X.; Dai, L.; Xu, Y. Holey graphene-based nanocomposites for efficient electrochemical energy storage. *Nano Energy* **2020**, *73*, No. 104762.

(8) Yan, B.; Chen, Z.; Xu, Y. Amorphous and Crystalline 2D Polymeric Carbon Nitride Nanosheets for Photocatalytic Hydrogen/Oxygen Evolution and Hydrogen Peroxide Production. *Chem. - Asian J.* **2020**, *15*, 2329−2340.

(9) Deb Nath, N. C.; Shah, S. S.; Qasem, M. A. A.; Zahir, M. H.; Aziz, M. A. Defective Carbon Nanosheets Derived from *Syzygium cumini* Leaves for Electrochemical Energy-Storage. *ChemistrySelect* **2019**, *4*, 9079−9083.

(10) Mohamedkhair, A. K.; Aziz, M. A.; Shah, S. S.; Shaikh, M. N.; Jamil, A. K.; Qasem, M. A. A.; Buliyaminu, I. A.; Yamani, Z. H. Effect of an activating agent on the physicochemical properties and supercapacitor performance of naturally nitrogen-enriched carbon derived from *Albizia procera* leaves. *Arabian J. Chem.* **2020**, *13*, 6161−6173.

(11) Augustyn, V.; Simon, P.; Dunn, B. Pseudocapacitive oxide materials for high-rate electrochemical energy storage. *Energy Environ. Sci.* **2014**, *7*, 1597−1614.

(12) Jiang, Y.; Liu, J. Definitions of Pseudocapacitive Materials: A Brief Review. *Energy Environ. Mater.* **2019**, *2*, 30−37.

(13) Abdah, M. A. A. M.; Azman, N. H. N.; Kulandaivalu, S.; Sulaiman, Y. Review of the use of transition-metal-oxide and conducting polymer-based fibres for high-performance supercapacitors. *Mater. Des.* **2020**, *186*, No. 108199.

(14) An, C.; Zhang, Y.; Guo, H.; Wang, Y. Metal oxide-based supercapacitors: progress and prospectives. *Nanoscale Adv.* **2019**, *1*, 4644−4658.

(15) Zhang, Y.; Li, L.; Su, H.; Hunag, W.; Dong, X. Binary metal oxide: advanced energy storage materials in supercapacitors. *J. Mater. Chem. A* **2015**, *3*, 43−59.

(16) Zhong, Y.; Xia, X.; Shi, F.; Zhan, J.; Tu, J.; Fan, H. J. Transition Metal Carbides and Nitrides in Energy Storage and Conversion. *Adv. Sci.* **2016**, *3*, No. 1500286.

(17) Shi, F.; Li, L.; Wang, X.-L.; Gu, C.-d.; Tu, J.-p. Metal oxide/hydroxide-based materials for supercapacitors. *RSC Adv.* **2014**, *4*, 41910−41921.

(18) Rui, X.; Tan, H.; Yan, Q. Nanostructured metal sulfides for energy storage. *Nanoscale* **2014**, *6*, 9889−9924.

(19) Fong, K. D.; Wang, T.; Smoukov, S. K. Multidimensional performance optimization of conducting polymer-based supercapacitor electrodes. *Sustainable Energy Fuels* **2017**, *1*, 1857−1874.

(20) Shah, S. S.; Alfasane, M. A.; Bakare, I. A.; Aziz, M. A.; Yamani, Z. H. Polyaniline and heteroatoms−enriched carbon derived from Pithophora polymorpha composite for high performance supercapacitor. *J. Energy Storage* **2020**, *3*, No. 101562.

(21) Zhang, Z.; Su, X.; Zhu, Y.; Fang, Z.; Luo, X.; Chen, Z. Polypyrrole encapsulation-protected porous multishelled Co_3O_4 hollow microspheres for advanced all-solid-state asymmetric supercapacitors with boosted reaction kinetics and stability. *Nanotechnology* **2020**, *31*, No. 255403.

(22) Chen, Z.; Li, S.; Zhao, Y.; Aboud, M. F. A.; Shakir, I.; Xu, Y. Ultrafine FeS2 nanocrystals/porous nitrogen-doped carbon hybrid nanospheres encapsulated in three-dimensional graphene for simultaneous efficient lithium and sodium ion storage. *J. Mater. Chem. A* **2019**, *7*, 26342−26350.

(23) Ozoliņŝ, V.; Zhou, F.; Asta, M. Ruthenia-Based Electrochemical Supercapacitors: Insights from First-Principles Calculations. *Acc. Chem. Res.* **2013**, *46*, 1084−1093.

(24) Sivaram, H.; Selvakumar, D.; Alsalme, A.; Alswieleh, A.; Jayavel, R. Enhanced performance of PbO nanoparticles and PbO-CdO and PbO-ZnO nanocomposites for supercapacitor application. *J. Alloys Compd.* **2018**, *731*, 55−63.

(25) Zhang, J.; Liu, F.; Cheng, J. P.; Zhang, X. B. Binary Nickel–Cobalt Oxides Electrode Materials for High-Performance Supercapacitors: Influence of its Composition and Porous Nature. *ACS Appl. Mater. Interfaces* **2015**, *7*, 17630–17640.

(26) Qi, Z.; Younis, A.; Chu, D.; Li, S. A Facile and Template-Free One-Pot Synthesis of Mn_3O_4 Nanostructures as Electrochemical Supercapacitors. *Nano-Micro Lett.* **2016**, *8*, 165–173.

(27) Barai, H. R.; Rahman, M. M.; Roy, M.; Barai, P.; Joo, S. W. A calcium doped binary strontium-copper oxide electrode material for high-performance supercapacitors. *Mater. Sci. Semicond. Process.* **2019**, *90*, 245–251.

(28) Ghodbane, O.; Pascal, J.-L.; Favier, F. Microstructural Effects on Charge-Storage Properties in MnO_2-Based Electrochemical Supercapacitors. *ACS Appl. Mater. Interfaces* **2009**, *1*, 1130–1139.

(29) Shao, P. R.; Deng, S. Z.; Chen, J.; Chen, J.; Xu, N. S. Study of field emission, electrical transport, and their correlation of individual single CuO nanowires. *J. Appl. Phys.* **2011**, *109*, No. 023710.

(30) Moosavifard, S. E.; El-Kady, M. F.; Rahmanifar, M. S.; Kaner, R. B.; Mousavi, M. F. Designing 3D Highly Ordered Nanoporous CuO Electrodes for High-Performance Asymmetric Supercapacitors. *ACS Appl. Mater. Interfaces* **2015**, *7*, 4851–4860.

(31) Senthilkumar, V.; Kim, Y. S.; Chandrasekaran, S.; Rajagopalan, B.; Kim, E. J.; Chung, J. S. Comparative supercapacitance performance of CuO nanostructures for energy storage device applications. *RSC Adv.* **2015**, *5*, 20545–20553.

(32) Huang, Y.-Y.; Lin, L.-Y. Synthesis of Ternary Metal Oxides for Battery-Supercapacitor Hybrid Devices: Influences of Metal Species on Redox Reaction and Electrical Conductivity. *ACS Appl. Energy Mater.* **2018**, *1*, 2979–2990.

(33) Chen, S.; Xing, W.; Duan, J.; Hu, X.; Qiao, S. Z. Nanostructured morphology control for efficient supercapacitor electrodes. *J. Mater. Chem. A* **2013**, *1*, 2941–2954.

(34) Zhi, M.; Xiang, C.; Li, J.; Li, M.; Wu, N. Nanostructured carbon–metal oxide composite electrodes for supercapacitors: a review. *Nanoscale* **2013**, *5*, 72–88.

(35) Lee, M.-T.; Chang, J.-K.; Tsai, W.-T.; Lin, C.-K. In situ X-ray absorption spectroscopic studies of anodically deposited binary Mn–Fe mixed oxides with relevance to pseudocapacitance. *J. Power Sources* **2008**, *178*, 476–482.

(36) Wang, Z.; Zhu, J.; Sun, P.; Zhang, P.; Zeng, Z.; Liang, S.; Zhu, X. Nanostructured Mn–Cu binary oxides for supercapacitor. *J. Alloys Compd.* **2014**, *598*, 166–170.

(37) Yuan, C.; Hou, L.; Li, D.; Zhang, Y.; Xiong, S.; Zhang, X. Unusual electrochemical behavior of Ru–Cr binary oxide-based aqueous symmetric supercapacitors in KOH solution. *Electrochim. Acta* **2013**, *88*, 654–658.

(38) Chen, L. Y.; Hou, Y.; Kang, J. L.; Hirata, A.; Fujita, T.; Chen, M. W. Toward the Theoretical Capacitance of RuO_2 Reinforced by Highly Conductive Nanoporous Gold. *Adv. Energy Mater.* **2013**, *3*, 851–856.

(39) Fan, X.; Sun, Y.; Ohlckers, P.; Chen, X. Porous Thin-Wall Hollow Co_3O_4 Spheres for Supercapacitors with High Rate Capability. *Appl. Sci.* **2019**, *9*, No. 4672.

(40) Barai, H. R.; Lopa, N. S.; Barai, P.; Rahman, M. M.; Sarker, A. K.; Joo, S. W. Binary strontium–copper oxide nanostructures doped with potassium as electrode material for supercapacitor application. *J. Mater. Sci.: Mater. Electron.* **2019**, *30*, 21269–21277.

(41) Zhang, S.; Liu, G.; Qiao, W.; Wang, J.; Ling, L. Oxygen vacancies enhance the lithium ion intercalation pseudocapacitive properties of orthorhombic niobium pentoxide. *J. Colloid Interface Sci.* **2020**, *562*, 193–203.

(42) Chen, X.; Chen, C.; Xu, T.; Xu, Y.; Liu, W.; Yang, W.; Yang, P. Performance enhancement of asymmetric supercapacitors with bud-like Cu-doped Mn_3O_4 hollow and porous structures on nickel foam as positive electrodes. *RSC Adv.* **2018**, *8*, 35878–35887.

(43) Sukhdev, A.; Challa, M.; Narayani, L.; Manjunatha, A. S.; Deepthi, P. R.; Angadi, J. V.; Kumar, P. M.; Pasha, M. Synthesis, phase transformation, and morphology of hausmannite Mn_3O_4 nanoparticles: photocatalytic and antibacterial investigations. *Heliyon* **2020**, *6*, No. e03245.

(44) Zhang, J.; Feng, H.; Qin, Q.; Zhang, G.; Cui, Y.; Chai, Z.; Zheng, W. Interior design of three-dimensional CuO ordered architectures with enhanced performance for supercapacitors. *J. Mater. Chem. A* **2016**, *4*, 6357–6367.

(45) Niu, X.; Wei, H.; Tang, K.; Liu, W.; Zhao, G.; Yang, Y. Solvothermal synthesis of 1D nanostructured Mn_2O_3: effect of Ni^{2+} and Co^{2+} substitution on the catalytic activity of nanowires. *RSC Adv.* **2015**, *5*, 66271–66277.

(46) Acharyya, S. S.; Ghosh, S.; Sharma, S. K.; Bal, R. Cetyl alcohol mediated fabrication of forest of Ag/Mn_3O_4 nanowhiskers catalyst for the selective oxidation of styrene with molecular oxygen. *RSC Adv.* **2015**, *5*, 89879–89887.

(47) Prakash, O.; Kumar, S.; Singh, P.; Deckert, V.; Chatterjee, S.; Ghosh, A. K.; Singh, R. K. Surface-enhanced Raman scattering characteristics of CuO:Mn/Ag heterojunction probed by methyl orange: effect of Mn^{2+} doping. *J. Raman Spectrosc.* **2016**, *47*, 813–818.

(48) Rashad, M.; Rüsing, M.; Berth, G.; Lischka, K.; Pawlis, A. CuO and Co_3O_4 Nanoparticles: Synthesis, Characterizations, and Raman Spectroscopy. *J. Nanomater.* **2013**, *2013*, No. 714853.

(49) Vázquez-Olmos, A.; Redón, R.; Rodríguez-Gattorno, G.; Mata-Zamora, M. E.; Morales-Leal, F.; Fernández-Osorio, A. L.; Saniger, J. M. One-step synthesis of Mn_3O_4 nanoparticles: Structural and magnetic study. *J. Colloid Interface Sci.* **2005**, *291*, 175–180.

(50) Lopa, N. S.; Rahman, M. M.; Ahmed, F.; Sutradhar, S. C.; Ryu, T.; Kim, W. A Ni-based redox-active metal-organic framework for sensitive and non-enzymatic detection of glucose. *J. Electroanal. Chem.* **2018**, *822*, 43–49.

(51) Bayram, O.; Guney, H.; Ertargin, M. E.; Igman, E.; Simsek, O. Effect of doping concentration on the structural and optical properties of nanostructured Cu-doped Mn_3O_4 films obtained by SILAR technique. *Appl. Phys. A* **2018**, *124*, No. 606.

(52) Raj, B. G. S.; Ramprasad, R. N. R.; Asiri, A. M.; Wu, J. J.; Anandan, S. Ultrasound assisted synthesis of Mn_3O_4 nanoparticles anchored graphene nanosheets for supercapacitor applications. *Electrochim. Acta* **2015**, *156*, 127–137.

(53) Fei, X.; Shao, Z.; Chen, X. Synthesis of hierarchical three-dimensional copper oxide nanostructures through a biomineralization-inspired approach. *Nanoscale* **2013**, *5*, 7991–7997.

(54) Chaki, S. H.; Tailor, J. P.; Deshpande, M. P. Synthesis and Characterizations of Undoped and Mn Doped CuS Nanoparticles. *Adv. Sci. Lett.* **2014**, *20*, 959–965.

(55) Hashem, A. M.; Abuzeid, H. M.; Mikhailova, D.; Ehrenberg, H.; Mauger, A.; Julien, C. M. Structural and electrochemical properties of α-MnO_2 doped with cobalt. *J. Mater. Sci.* **2012**, *47*, 2479–2485.

(56) Su, D.; Xie, X.; Dou, S.; Wang, G. CuO single crystal with exposed {001} facets - A highly efficient material for gas sensing and Li-ion battery applications. *Sci. Rep.* **2014**, *4*, No. 5753.

(57) Anil, C.; Madras, G. Kinetics of CO oxidation over Cu doped Mn_3O_4. *J. Mol. Catal. A: Chem.* **2016**, *424*, 106–114.

(58) Dong, R.; Ye, Q.; Kuang, L.; Lu, X.; Zhang, Y.; Zhang, X.; Tan, G.; Wen, Y.; Wang, F. Enhanced Supercapacitor Performance of Mn_3O_4 Nanocrystals by Doping Transition-Metal Ions. *ACS Appl. Mater. Interfaces* **2013**, *5*, 9508–9516.

(59) Zhao, Y.; Ikram, M.; Zhang, J.; Kan, K.; Wu, H.; Song, W.; Li, L.; Shi, K. Outstanding gas sensing performance of CuO-CNTs nanocomposite based on asymmetrical schottky junctions. *Appl. Surf. Sci.* **2018**, *428*, 415–421.

(60) Huang, J.; Wu, H.; Cao, D.; Wang, G. Influence of Ag doped CuO nanosheet arrays on electrochemical behaviors for supercapacitors. *Electrochim. Acta* **2012**, *75*, 208–212.

(61) An, G.; Wu, P.; Xiao, M.; Liu, Z.; Miao, Z.; Ding, K.; Mao, L. Low-temperature synthesis of Mn_3O_4 nanoparticles loaded on multi-walled carbon nanotubes and their application in electrochemical capacitors. *Nanotechnology* **2008**, *19*, No. 275709.